Electronic Supplementary Material (ESI) for Inorganic Chemistry Frontiers.

Supporting Information

New members of radical bridged Ln_2 metallocene single-molecule magnets based on the unsubstituted 1,2,4,5-tetrazine ligand

Niki Mavragani,[†] Alexandros A. Kitos,[†] Akseli Mansikkamäki[‡] and Muralee Murugesu*[†]

Table of Contents:

[†] *Department of Chemistry and Biomolecular Sciences, University of Ottawa, 10 Marie Curie, Ottawa, Ontario, K1N 6N5, Canada.*
E-mail: m.murugesu@uottawa.ca
[‡] *NMR Research Unit, University of Oulu, P.O. Box 300, 90014 Oulu, Finland.*

1. Experimental Section

General Procedures and Materials: All operations were performed in an Mbraun glovebox under an N_2 atmosphere. Solvents were dried using a J. C. Meyer solvent system, degassed by free-pump-thaw method and stored over activated 3 Å molecular sieves prior to use. The 1,2,4,5-tetrazine (tz) ligand was prepared according to the literature.[1] [Cp^*_2Ln][(μ-Ph_2)BPh_2] (Ln = Dy^{III}, Tb^{III} and Gd^{III}) starting materials were prepared according to the literature.[2] All reagents and solvents were purchased from TCI, Alfa Aesar, or Strem Chemicals and used without further purification. HCp* (99+%) was purchased from Alfa Aesar and was degassed/dried as previously described prior to use. FT-IR spectra were recorded on a Nicolet Nexus 550 FT-IR spectrometer in the transmission window of 400-4000 cm^{-1}. Elemental Analysis was performed by Midwest Microlab.

Synthesis of [($Cp^*_2Gd)_2(tz^{\bullet-})(THF)_2$][$BPh_4$] (1): To a solution of tz (0.125 mmol, 10 mg) in THF (5 mL), one equivalent of KC_8 (0.125 mmol, 17 mg) was added. After ~ 5 h, the dark grey colour mixture was slowly added to a solution of two equivalents of [(Cp^*_2Gd][(μ-Ph_2)(BPh_2)] (0.25 mmol, 187 mg) in THF (5 mL). The resulting dark red mixture was left to stir overnight and then filtered. Upon slow diffusion with Et_2O, dark red crystals of **1** were isolated after two days in 63 % yield. Selected IR bands (cm^{-1}): 3053.16 (w), 2908.83 (m), 2854.82 (m), 1580.28 (w), 1478.78 (m), 1434.07 (s), 1377.76 (m), 1217.82 (s), 1182.55 (w), 1093.31 (m), 1066.08 (m), 1012.98 (s), 917.18 (w), 887.07 (m), 859.07 (s), 839.85 (s), 731.29 (s), 740.85 (vs), 702.96 (vs), 648.55 (m), 614.42 (s), 604.90 (m), 585.66 (m), 568.60 (w), 536.77 (w). Elemental Analysis: Complex **1** was analyzed as solvent free: Calcd: C, 63.44 %; H, 7.05 %; N, 3.99%, Found: C, 62.91%; H, 7.52%; N, 4.09%.

Synthesis of [($Cp^*_2Tb)_2(tz^{\bullet-})(THF)_2$][$BPh_4$] (2) and [($Cp^*_2Dy)_2(tz^{\bullet-})(THF)_2$][$BPh_4$] (3):These complexes were prepared in a similar manner as **1** by simply replacing [Cp^*_2Gd][(μ-Ph_2)BPh_2] with [Cp^*_2Tb][(μ-Ph_2)BPh_2] (0.25 mmol, 187 mg) in **2** and [Cp^*_2Dy][(μ-Ph_2)BPh_2] (0.25 mmol, 188 mg) in **3**. Yields = 62-67%. Elemental Analysis: Complex **2** was analyzed as **2**·$2Et_2O$: Calcd: C, 63.60%; H, 7.42%; N, 3.62 %, Found: C, 64.31 %; H, 7.42%; N, 3.62 %. Selected IR bands (cm^{-1}) for **2**: 3050.14 (w), 2972.14 (m), 2857.56 (m), 1580.02 (w), 1478.67 (m), 1433.92 (s), 1378.83 (m), 1237.34 (m), 1217.45 (s), 1182.65 (w), 1003.13 (w), 1067.36 (m), 1013.47 (s), 916.00 (w), 859.08 (s), 839.76 (s), 740.22 (s), 730.61 (s), 703.54 (vs), 625.45 (w), 614.54 (s), 557.86 (w), 549.98 (w). Elemental Analysis: Complex **3** was analyzed as solvent free: Calcd: C, 62.97 %; H, 6.99 %; N, 3.96 %, Found: C, 62.68 %; H, 7.63 %; N, 4.02 %. Selected IR bands (cm^{-1}) for **3**: 3053.64 (w), 2973.52 (m), 2858.74 (m), 1580.28 (w), 1472.82 (m), 1434.07 (s), 1378.36 (m), 1217.41 (s), 1182.33 (w), 1152.49 (w), 1119.16 (m), 1093.43 (m), 1066.29 (s), 1013.73 (s), 916.11 (w), 888.40 (w), 859.08 (s), 840.35 (s), 740.00 (s), 730.99 (s), 703.22 (vs), 652.32 (m), 614.37 (s), 604.73 (s), 533.74 (w).

Single Crystal X-ray Diffraction: Suitable crystals for single-crystal X-ray diffraction (SCXRD) analysis were covered in parabar oil and mounted on a thin glass fiber. Full data (Table S1) were collected on a Bruker KAPPA APEX-II CCD single-crystal diffractometer (graphite monochromated Mo-Kα radiation, λ = 0.71073 Å), at 203 K temperature. Absorption corrections were applied by using multi-scan of the SADABS[3] program. Structures were solved using direct methods with SHELXT[4] and refined by the full-matrix least-squares methods on F^2 with SHELXL-2018/3[5] in anisotropic approximation for all non-hydrogen atoms. Carbon-bound hydrogen atoms were included in calculated positions (see details in the CIF files). The crystal structures of **1**, **2** and **3** contain an area of highly disordered solvent molecules (mostly diethyl ether molecules with partial occupancies) resulting in a smeared-out electron density. Attempts to model the disordered areas with chemically and crystallographic reasonable geometries were unsuccessful and therefore, the SQUEEZE[6] function of PLATON[7] was used to remove the contribution of the electron density associated with those molecules from the intensity data. All geometric/crystallographic calculations were carried out using WINGX[8] package while the molecular/packing graphics were prepared with DIAMOND[9] and MERCURY.[10] For comparison purposes, a similar labelling scheme was applied in all structures.

Magnetic Measurements: Magnetic susceptibility measurements were obtained using a Quantum Design SQUID magnetometer MPMS-XL7 operating between 1.8 and 300 K. Direct current (dc) measurements were performed on 15.3 mg (**1**), 15.5 mg (**2**) and 17.3 mg (**3**) of crushed polycrystalline samples, which were restrained with silicon grease and sealed in a polyethylene membrane under an inert atmosphere for which diamagnetic corrections were applied. The samples were subjected to dc fields of 7 to -7 T while alternating current (ac) measurements took place under zero field.

2. Single-crystal X-ray data and molecular features

Table S1. Crystallographic data and details for **1**, **2** and **3**.

Compound reference	1	2	3
Chemical formula	$C_{74}H_{98}BGd_2N_4O_2$	$C_{74}H_{98}BN_4O_2Tb_2$	$C_{74}H_{98}BDy_2N_4O_2$
Formula mass	1400.87	1404.21	1411.37
Crystal system	Monoclinic	Monoclinic	Monoclinic
a/Å	15.3219(5)	15.2603(8)	15.2675(6)
b/Å	20.3671(6)	20.2689(11)	20.2943(8)
c/Å	25.4887(8)	25.5427(14)	25.5113(12)
α/°	90	90	90
β/°	96.429(2)	96.330(3)	96.393(3)
γ/°	90	90	90
Unit cell volume/Å^3	7904.0(4)	7852.4(7)	7855.3(6)
Temperature/K	203(2)	203(2)	203(2)
Space group	I2/a	I2/a	I2/a
No. of formula units/unit cell, *Z*	4	4	4
Radiation type	Mo Kα	Mo Kα	Mo Kα
Absorption coefficient, *μ*/mm^{-1}	1.704	1.827	1.928
No. of reflections measured	66087	70044	52187
No. of independent reflections	7774	8587	8592
R_{int}	0.0367	0.0315	0.0539
Final R_1 values (all data)	0.0461	0.0362	0.0415
Final $wR_2(F^2)$ values (all data)	0.0792	0.0634	0.0642
Final R_1 values ($I > 2\sigma(I)$)	0.0354	0.0265	0.0268
Final $wR_2(F^2)$ values ($I > 2\sigma(I)$)	0.0722	0.0578	0.0597
Goodness of fit on F^2	1.046	1.029	1.014
CCDC number	2202463	2202464	2202465

Table S2. Selected distances (Å) and angles (º) for **1**, **2** and **3**. Symmetry related atoms are indicated (').

Distance/angle		Distance/angle	
1			
Gd-Gd'	7.132(5)	Gd-O	2.403(2)
Gd-N1	2.467(3)	Gd-N2'	2.503(3)
Gd-Cp_{cent}*A	2.428(5)	Gd-Cp_{cent}*B	2.427(4)
Gd-tz_{cent}	3.566(4)	N1-N2'	1.392(4)
O-Gd-Cp_{cent}*A	103.1(6)	O-Gd-Cp_{cent}*B	101.9(6)
N1-Gd-Cp_{cent}*A	99.9(8)	N1-Gd-N2'	32.5(9)
N2-Gd-Cp_{cent}*A	107.7(8)	N1-Gd-Cp_{cent}*B	102.0(7)
Cp_{cent}*A-Gd-Cp_{cent}*B	136.3(2)	N2-Gd-Cp_{cent}*B	111.1(7)
2			
Tb-Tb'	7.088(6)	Tb-O	2.388(2)
Tb-N1	2.453(2)	Tb-N2'	2.485(2)
Tb-Cp_{cent}*A	2.408(5)	Tb-Cp_{cent}*B	2.402(4)
Tb-tz_{cent}	3.544(4)	N1-N2'	1.394(3)
O-Tb-Cp_{cent}*A	103.1(5)	O-Tb-Cp_{cent}*B	101.7(5)
N1-Tb-Cp_{cent}*A	99.8(6)	N1-Tb-N2'	32.8(7)
N2-Tb-Cp_{cent}*A	107.7(6)	N1-Tb-Cp_{cent}*B	102.0(5)
Cp_{cent}*A-Tb-Cp_{cent}*B	136.4(2)	N2-Tb-Cp_{cent}*B	111.1(5)
3			
Dy-Dy'	7.077(5)	Dy-O	2.376(2)
Dy-N1	2.445(2)	Dy-N2'	2.475(2)
Dy-Cp_{cent}*A	2.396(5)	Dy-Cp_{cent}*B	2.394(4)
Dy-tz_{cent}	3.538(4)	N1-N2'	1.391(3)
O-Dy-Cp_{cent}*A	102.9(5)	O-Dy-Cp_{cent}*B	101.8(5)
N1-Dy-Cp_{cent}*A	100.0(6)	N1-Dy-N2'	32.8(7)
N2-Dy-Cp_{cent}*A	107.7(6)	N1-Dy-Cp_{cent}*B	101.8(5)
Cp_{cent}*A-Dy-Cp_{cent}*B	136.6(2)	N2-Dy-Cp_{cent}*B	111.0(5)

Cp_{cent}*A: C6-C15, Cp_{cent}*B: C16-C25

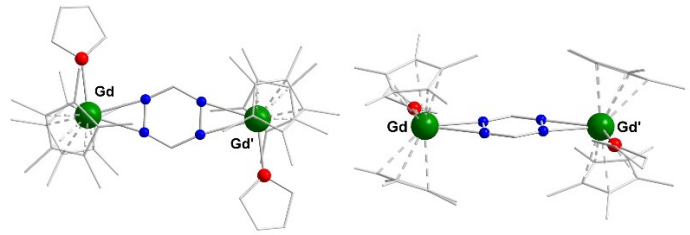

$[(Cp^*_2Gd^{III})_2(tz^{\bullet-})(THF)_2](BPh_4)$

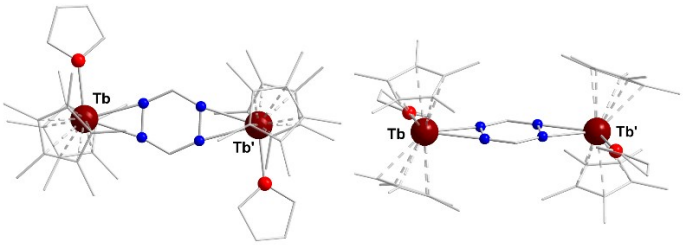

$[(Cp^*_2Tb^{III})_2(tz^{\bullet-})(THF)_2](BPh_4)$

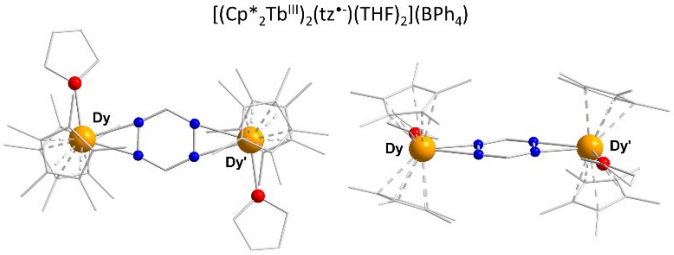

$[(Cp^*_2Dy^{III})_2(tz^{\bullet-})(THF)_2](BPh_4)$

Fig. S1: Molecular structures of complexes **1** (top), **2** (middle) and **3** (bottom). For clarity reasons BPh_4^- moieties as well as H-atoms have been omitted.

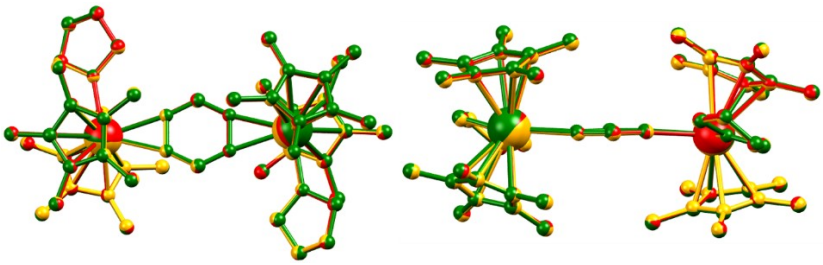

Fig. S2: Top (left) and side view (right) of the molecular overlay of the isomorphic complexes **1** (green), **2** (red) and **3** (orange). The fit was performed over the metal centers; r.m.s. deviation: 0.0258 Å.

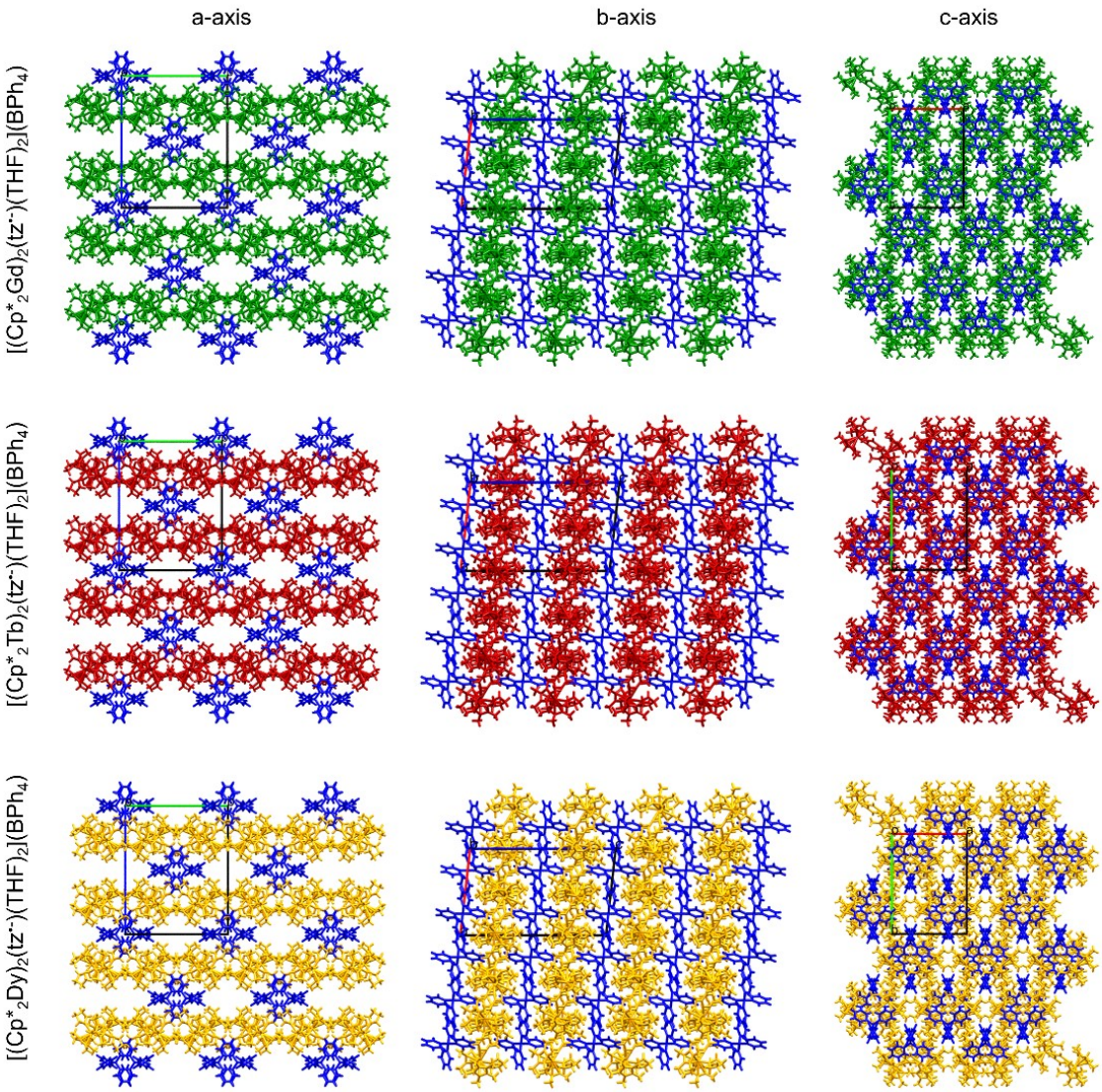

Fig. S3: Packing diagrams along a-, b- and c-axis of **[(Cp*$_2$Gd)$_2$(tz$^{\bullet-}$)(THF)$_2$](BPh$_4$)** (green), **[(Cp*$_2$Tb)$_2$(tz$^{\bullet-}$)(THF)$_2$](BPh$_4$)** (red) and **[(Cp*$_2$Dy)$_2$(tz$^{\bullet-}$)(THF)$_2$](BPh$_4$)** (orange) forming layers separated by BPh_4^- (blue) counterions.

3. Hirshfeld surface analysis and supramolecular organization

On the supramolecular level, the absence of strong hydrogen bonding donors or acceptors in both the main residue and solvent area of **1**, **2** and **3** leads mostly to close packing interactions such as C···H/H···C and H···H interactions.[11] This can be further supported by the Hirshfeld surface (HS) analysis,[12] using the Crystal Explorer software,[13] which shows that the main source of the supramolecular interactions on the d_{norm} surfaces (red spots) are the H-atoms of the coordinated THF molecules and the Cp^* ligands (Fig. S3). When the shape index function is applied to the HS, no "bow-tie" patterns or red/blue triangles observed indicating the complete absence of π···π stacking interactions (Fig. S3). The 2D fingerprint plots[14] of interatomic interactions (Fig. S4) show the percentages of all the contacts contributing to the total HS area of the molecules revealing that the H···H and C···H/H···C interactions dominating the surfaces with total percentages of 88% and 12%, as expected.

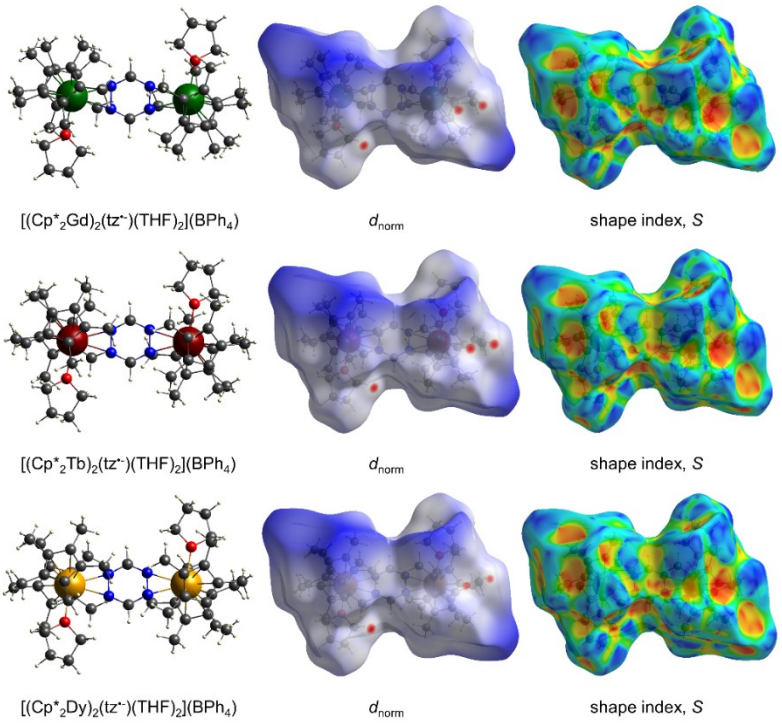

Fig. S3: Hirshfeld surface (HS) for **[(Cp*$_2$Gd)$_2$(tz$^{\bullet-}$)(THF)$_2$](BPh$_4$)** (top), **[(Cp*$_2$Tb)$_2$(tz$^{\bullet-}$)(THF)$_2$](BPh$_4$)** (middle) and **[(Cp*$_2$Dy)$_2$(tz$^{\bullet-}$)(THF)$_2$](BPh$_4$)** (bottom) mapped over d_{norm} and shape index, *S*. In the d_{norm} HS a red–blue–white colour scheme used where red regions represent closer contacts, blue regions represent longer contacts and white regions represent the distance of contacts which is exactly equal to the *vdW* separation.

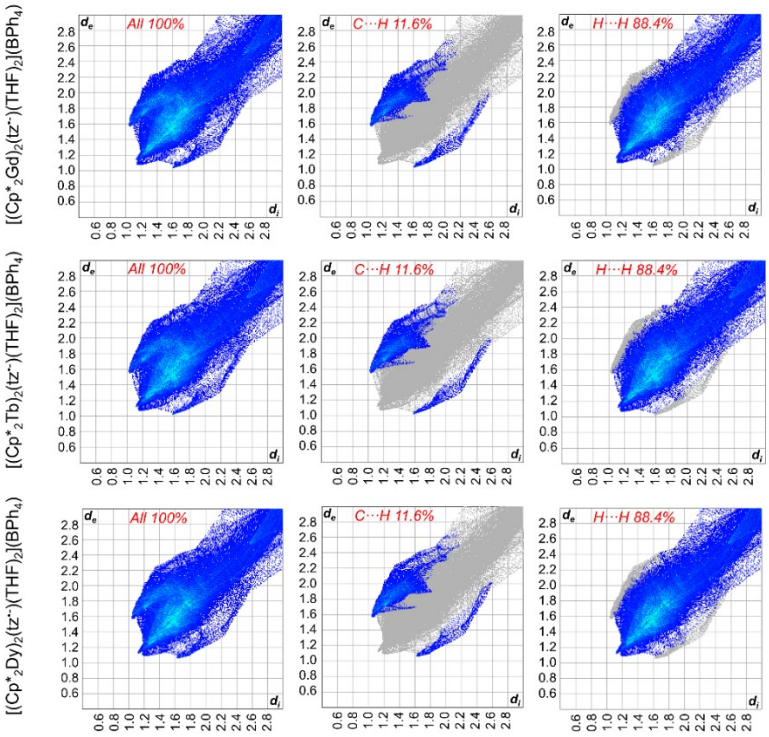

Fig. S4: The 2D fingerprint plots of interatomic interactions of **[(Cp*$_2$Gd)$_2$(tz$^{\bullet-}$)(THF)$_2$](BPh$_4$)** (top), **[(Cp*$_2$Tb)$_2$(tz$^{\bullet-}$)(THF)$_2$](BPh$_4$)** (middle) and **[(Cp*$_2$Dy)$_2$(tz$^{\bullet-}$)(THF)$_2$](BPh$_4$)** (bottom), showing the percentages of contacts contributed to the total Hirshfeld surface area of the molecules.

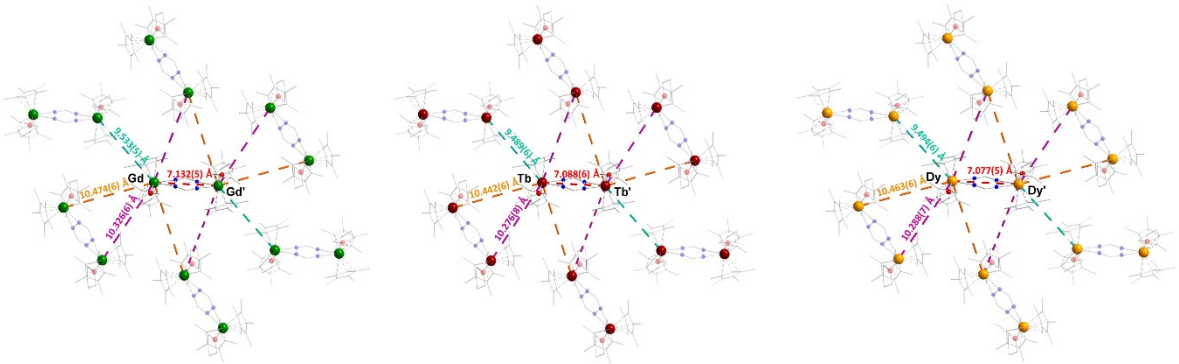

[(Cp*$_2$Gd^{III})$_2$(tz$^{\bullet-}$)(THF)$_2$](BPh$_4$) [(Cp*$_2$Tb^{III})$_2$(tz$^{\bullet-}$)(THF)$_2$](BPh$_4$) [(Cp*$_2$Dy^{III})$_2$(tz$^{\bullet-}$)(THF)$_2$](BPh$_4$)

Fig. S5: Intramolecular and intermolecular Ln···Ln distances for **1**-**3**. For clarity reasons, partial transparency has been employed and BPh$_4^-$ as well as H-atoms have been omitted. Each Ln···Ln distance is colour coded.

4. Additional magnetic data

DC Magnetism Plots for Complexes 2 and 3:

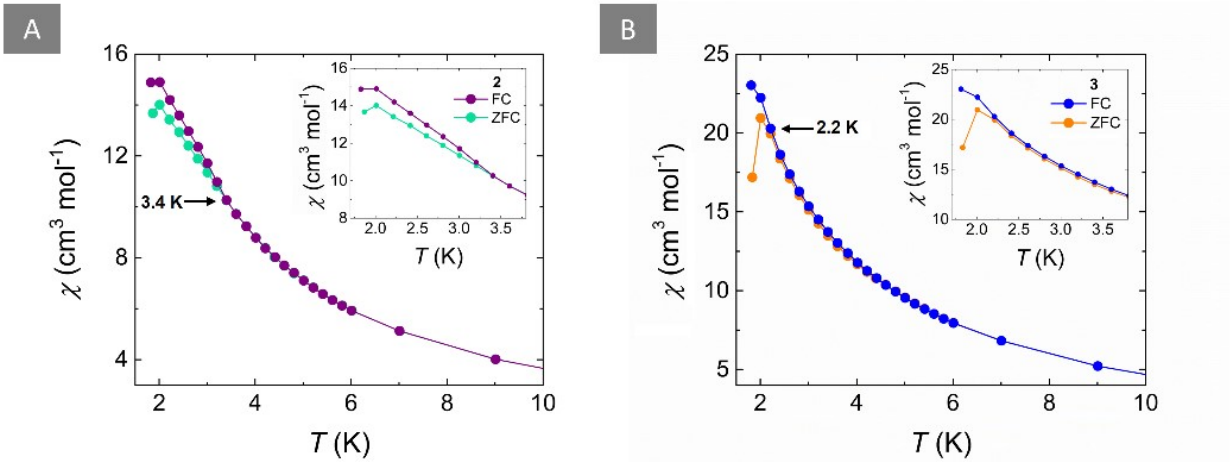

Fig. S7: Zero-field-cooled and field-cooled (ZFC/FC) curves for **2** (A) and **3** (B) under an applied static field of 1000 Oe. Data were collected at an average sweep rate of 0.2 K min^{-1}. ZFC and FC susceptibilities bifurcate at 3.4 K for **2** and 2.2 K for **3**, as indicated by the respective black arrows.

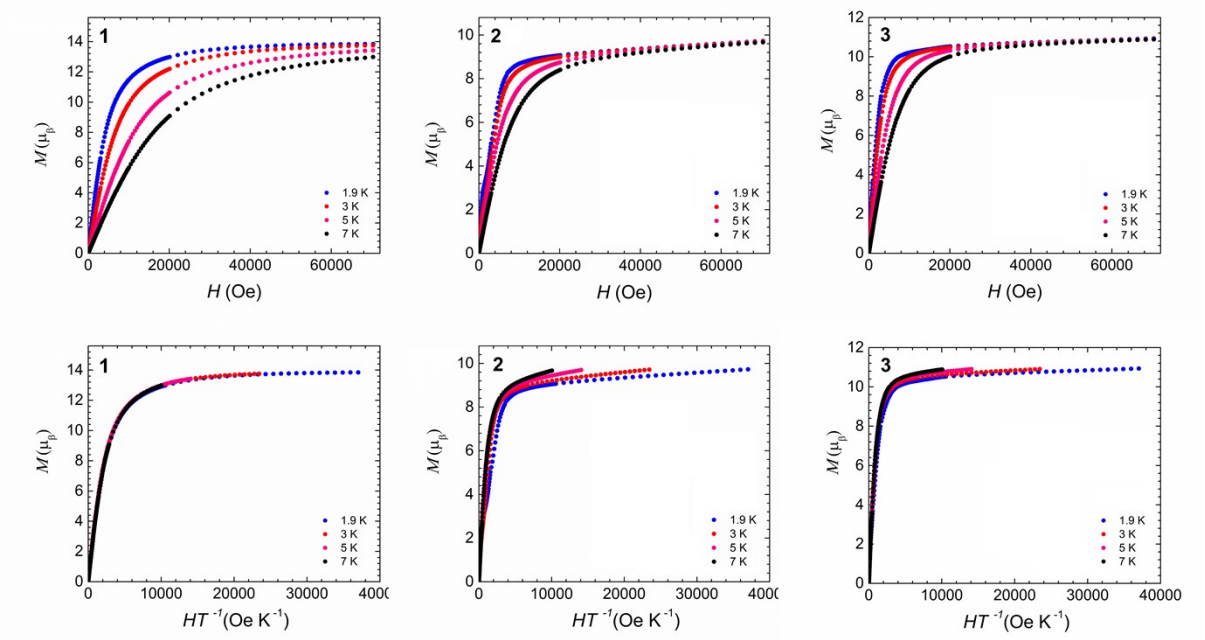

Fig. S8: Field dependence of the magnetization (top) and the reduced magnetization (bottom) for **1**-**3** at the indicated temperatures.

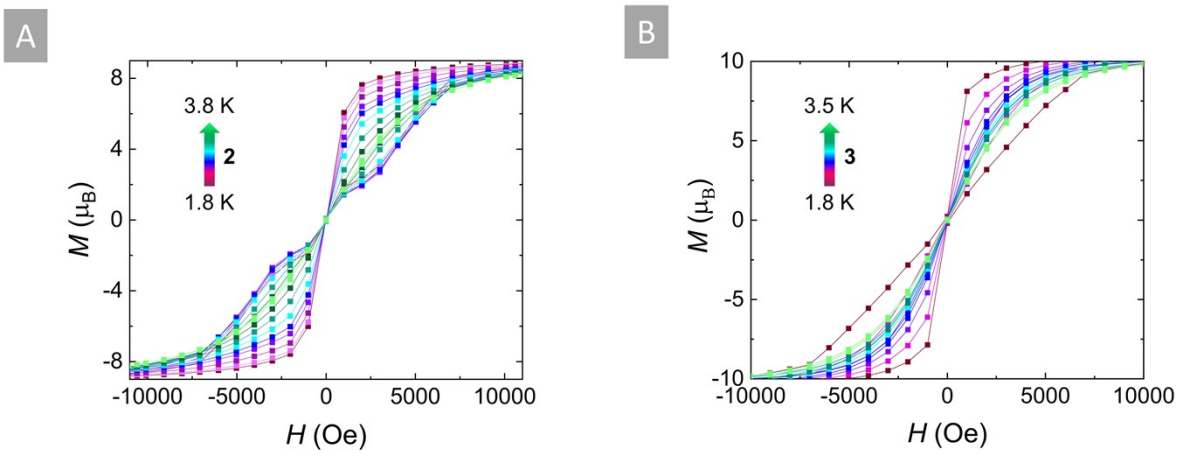

Fig. S9: Magnetic hysteresis data for **2** (A) and **3** (B) in the respective temperature ranges performed with an average sweep rate of 31 Oe/s.

AC Magnetism Plots for Complexes 2 and 3:

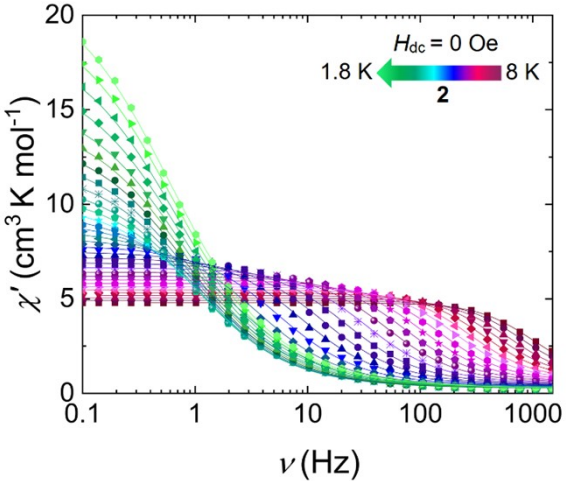

Fig. S10: Frequency dependence of χ' as a function of temperature in the 1.8-8 K temperature range, in the absence of an applied field (H_{dc} = 0 Oe) for **2**. Solid lines represent best fits to the generalized Debye model.

Table S3. Fitting parameters obtained from CCFit-2[15] using a generalized Debye model for the ac data of **2** in the absence of a static dc field (H_{dc} = 0 Oe) in the temperature region of 1.8 to 8 K (Fig. 3A, B, S10).

T (K)	τ (s)	α	χ_s (cm^3 mol^{-1})	χ_t(cm^3 mol^{-1})
1.8	0.27	0.32	0.26	22.2
2	0.26	0.31	0.26	20.6
2.2	0.24	0.30	0.26	18.9
2.4	0.23	0.30	0.27	17.2
2.6	0.21	0.29	0.27	15.8
2.8	0.20	0.28	0.26	14.7
3	0.19	0.28	0.26	13.7
3.2	0.18	0.27	0.26	12.8
3.4	0.18	0.27	0.26	12.0
3.6	0.17	0.27	0.26	11.3
3.8	0.16	0.26	0.27	10.1
4	0.14	0.26	0.28	10.0
4.2	0.12	0.26	0.30	9.66
4.4	9.20 x 10^{-2}	0.25	0.33	9.17
4.6	6.64 x 10^{-2}	0.24	0.36	8.70
4.8	4.47 x 10^{-2}	0.23	0.38	8.26
5	2.89 x 10^{-2}	0.22	0.40	7.87
5.2	1.83 x 10^{-2}	0.20	0.42	7.52
5.4	1.15 x 10^{-2}	0.20	0.44	7.21
5.6	7.35 x 10^{-3}	0.19	0.47	6.92
5.8	4.78 x 10^{-3}	0.17	0.50	6.66
6	3.18 x 10^{-3}	0.16	0.53	6.43
6.2	2.16 x 10^{-3}	0.15	0.55	6.21
6.4	1.51 x 10^{-3}	0.14	0.60	6.01
6.6	1.07 x 10^{-3}	0.13	0.62	5.83
6.8	7.80 x 10^{-4}	0.12	0.67	5.65
7	5.74 x 10^{-4}	0.10	0.70	5.48
7.2	4.32 x 10^{-4}	0.10	0.74	5.33
7.4	3.30 x 10^{-4}	0.09	0.78	5.19
7.6	2.57 x 10^{-4}	0.07	0.82	5.05
7.8	2.02 x 10^{-4}	0.06	0.87	4.91
8	1.61 x 10^{-4}	0.05	0.90	4.80

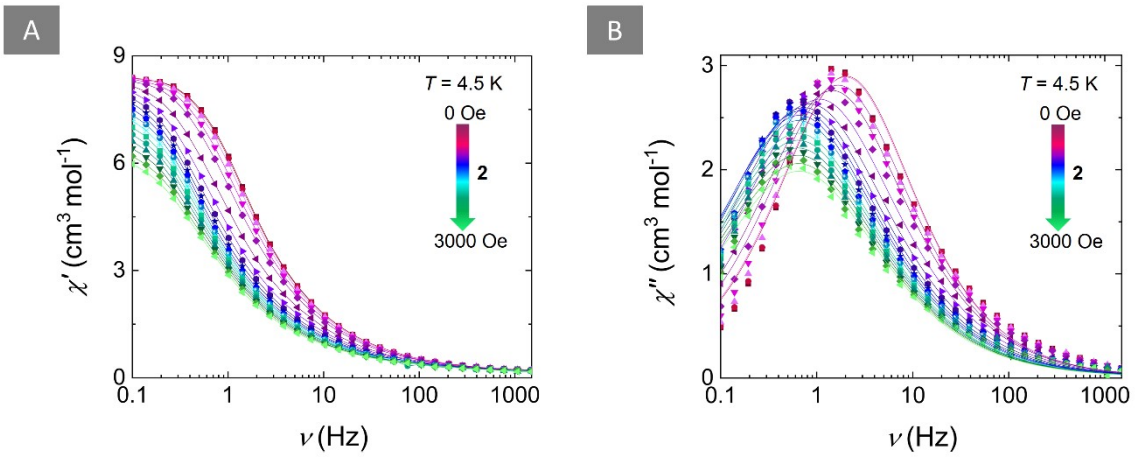

Fig. S11: Field dependence of the in-phase (χ') (A) and out-of-phase (χ'') (B) magnetic susceptibility of **2** at 4.5 K in the field range of 0 to 3000 Oe. For the χ' the solid lines serve as a guide to the eye, while for the χ'' the solid lines represent the best fit to the generalized Debye model.

Table S4. Best-fit parameters to the generalized Debye model for the frequency dependence of the out-of-phase-magnetic susceptibility (χ'') as a function of field for **2** collected at T = 4.5 K (Figure S11).

H (Oe)	τ (s)	α	χ_s (cm^3 mol^{-1})	χ_t (cm^3 mol^{-1})
0	7.85 x 10^{-2}	0.24	0.34	8.92
100	8.00 x 10^{-2}	0.25	0.34	8.93
200	8.52 x 10^{-2}	0.25	0.33	8.95
300	9.49 x 10^{-2}	0.27	0.31	8.98
400	1.09 x 10^{-1}	0.28	0.30	9.02
600	1.49 x 10^{-1}	0.31	0.28	9.11
800	1.88 x 10^{-1}	0.32	0.28	9.13
1000	2.16 x 10^{-1}	0.32	0.28	9.08
1200	2.33 x 10^{-1}	0.32	0.28	8.99
1400	2.42 x 10^{-1}	0.32	0.27	8.84
1600	2.47 x 10^{-1}	0.32	0.27	8.66
1800	2.49 x 10^{-1}	0.32	0.27	8.47
2000	2.49 x 10^{-1}	0.32	0.26	8.25
2200	2.49 x 10^{-1}	0.32	0.26	8.03
2400	2.50 x 10^{-1}	0.33	0.26	7.81
2600	2.48 x 10^{-1}	0.32	0.26	7.55
2800	2.47 x 10^{-1}	0.33	0.25	7.31
3000	2.44 x 10^{-1}	0.33	0.25	7.04

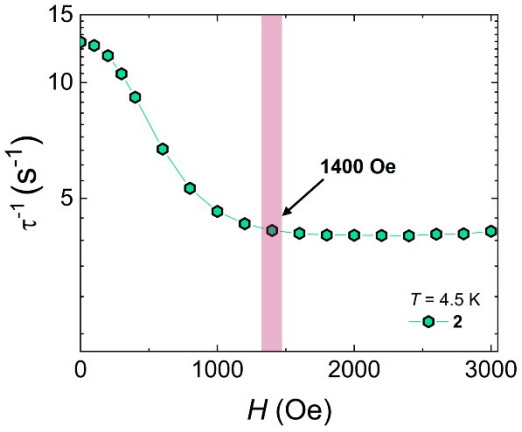

Fig. S12: Field-dependence of the relaxation times (τ) for **2** at a fixed temperature of 4.5 K. The relaxation times were obtained from the generalized Debye model (*see*, Table S4). The optimal static field for which the relaxation times of both processes are longest and quantum tunneling of the magnetization is reduced, is highlighted with a light-purple line. This is the field at which temperature dependent relaxation studies for **2** were completed at (*vide infra*).

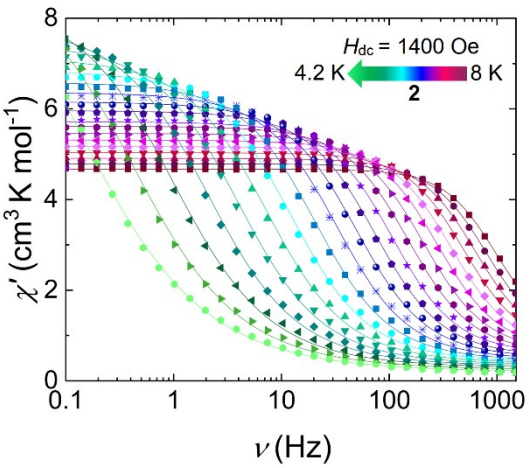

Fig. S13 Frequency dependence of χ' as a function of temperature in the 4.2-8 K temperature range, under an applied static field of 1400 Oe for **2**. Solid lines represent best fits to the generalized Debye model.

Table S5. Fitting parameters obtained from CCFit-2[15] using a generalized Debye model for the ac data of **2** in the presence of a static dc field (H_{dc} = 1400 Oe) in the temperature region of 4.2 to 8 K (Fig. 3D, E, S13).

T (K)	τ (s)	α	χ_s (cm^3 mol^{-1})	χ_t(cm^3 mol^{-1})
4.2	1.18	0.40	0.20	10.8
4.4	0.38	0.35	0.25	9.29
4.6	0.16	0.30	0.30	8.43
4.8	7.60 x 10^{-2}	0.27	0.33	7.88
5	3.97 x 10^{-2}	0.25	0.36	7.47
5.2	2.19 x 10^{-2}	0.23	0.38	7.13
5.4	1.28 x 10^{-2}	0.20	0.41	6.84
5.6	7.75 x 10^{-3}	0.19	0.43	6.59
5.8	4.88 x 10^{-3}	0.18	0.46	6.36
6	3.20 x 10^{-3}	0.17	0.50	6.16
6.2	2.15 x 10^{-3}	0.16	0.53	5.96
6.4	1.48 x 10^{-3}	0.13	0.60	5.72
6.6	1.06 x 10^{-3}	0.13	0.60	5.62
6.8	7.66 x 10^{-4}	0.12	0.63	5.46
7	5.63 x 10^{-4}	0.11	0.67	5.31
7.2	4.25 x 10^{-4}	0.10	0.72	5.17
7.4	3.23 x 10^{-4}	0.09	0.75	5.03
7.6	2.52 x 10^{-4}	0.08	0.80	4.91
7.8	1.97 x 10^{-4}	0.07	0.82	4.79
8	1.60 x 10^{-4}	0.05	0.90	4.67

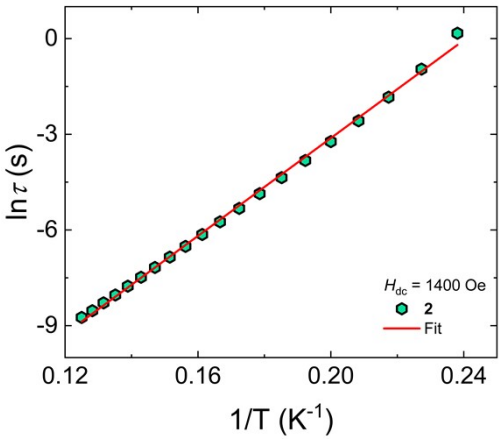

Fig. S14: The Arrhenius plot of the ln of the relaxation time, *τ*, of the magnetization *vs.* the inverse temperature for **2** under and applied field of 1400 Oe. The red line represents the linear fit to the Arrhenius equation that affords a U_{eff} = 53.3 cm^{-1}. Parameters are summarized in Table S5.

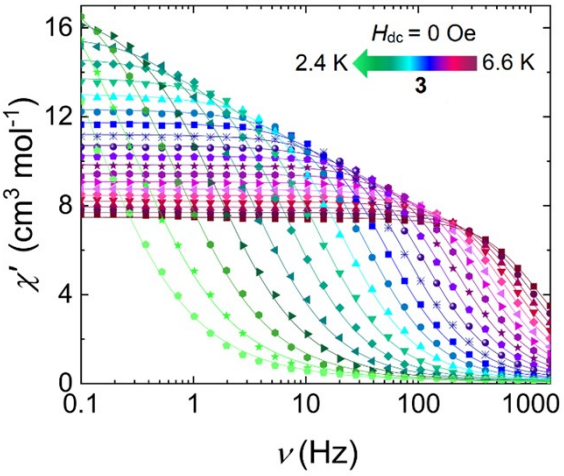

Fig. S15: Frequency dependence of *χ'* as a function of temperature in the 2.4-6.6 K temperature range, in the absence of an applied field (H_{dc} = 0 Oe) for **3**. Solid lines represent best fits to the generalized Debye model.

Table S6. Fitting parameters obtained from CCFit-2[15] using a generalized Debye model for the ac data of **3** in the absence of a static dc field (H_{dc} = 0 Oe) in the temperature region of 2.4 to 6.6 K (Fig. 3G, H, S15).

T (K)	τ (s)	α	χ_s (cm^3 mol^{-1})	χ_t(cm^3 mol^{-1})
2.4	1.23	0.30	9.95 x 10^{-2}	22.5
2.6	0.54	0.29	5.88 x 10^{-2}	20.6
2.8	0.22	0.27	5.30 x 10^{-2}	18.7
3	9.58 x 10^{-2}	0.24	6.50 x 10^{-2}	17.1
3.2	4.51 x 10^{-2}	0.21	7.10 x 10^{-2}	15.7
3.4	2.31 x 10^{-2}	0.19	7.26 x 10^{-2}	14.7
3.6	1.27 x 10^{-2}	0.18	7.64 x 10^{-2}	13.8
3.8	7.41 x 10^{-3}	0.17	7.85 x 10^{-2}	13.0
4	4.55 x 10^{-3}	0.16	8.77 x 10^{-2}	12.3
4.2	2.94 x 10^{-3}	0.15	0.10	11.8
4.4	1.98 x 10^{-3}	0.14	0.12	11.2
4.6	1.37 x 10^{-3}	0.13	0.14	10.7
4.78	9.87 x 10^{-4}	0.13	0.17	10.3
5	7.27 x 10^{-4}	0.12	0.20	9.84
5.2	5.51 x 10^{-4}	0.12	0.25	9.45
5.4	4.25 x 10^{-4}	0.11	0.28	9.08
5.6	3.35 x 10^{-4}	0.11	0.31	8.75
5.8	2.71 x 10^{-4}	0.10	0.39	8.47
6	2.21 x 10^{-4}	0.10	0.42	8.19
6.2	1.84 x 10^{-4}	0.09	0.46	7.94
6.4	1.53 x 10^{-4}	0.09	0.47	7.70
6.6	1.28 x 10^{-4}	0.09	0.44	7.48

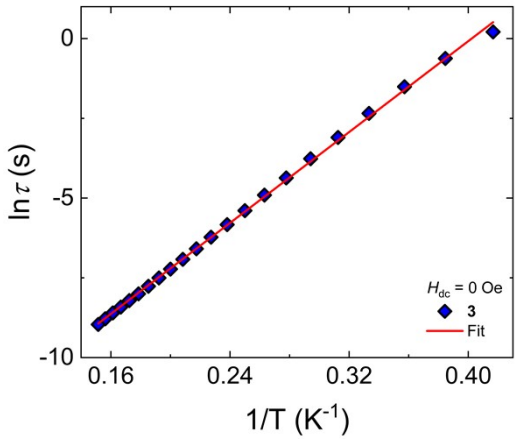

Fig. S16: The Arrhenius plot of the ln of the relaxation time, τ, of the magnetization *vs.* the inverse temperature for **3** in the absence of a static dc field (H_{dc} = 0 Oe). The red line represents the linear fit to the Arrhenius equation that affords a U_{eff} = 24.8 cm^{-1}. Parameters are summarized in Table S6.

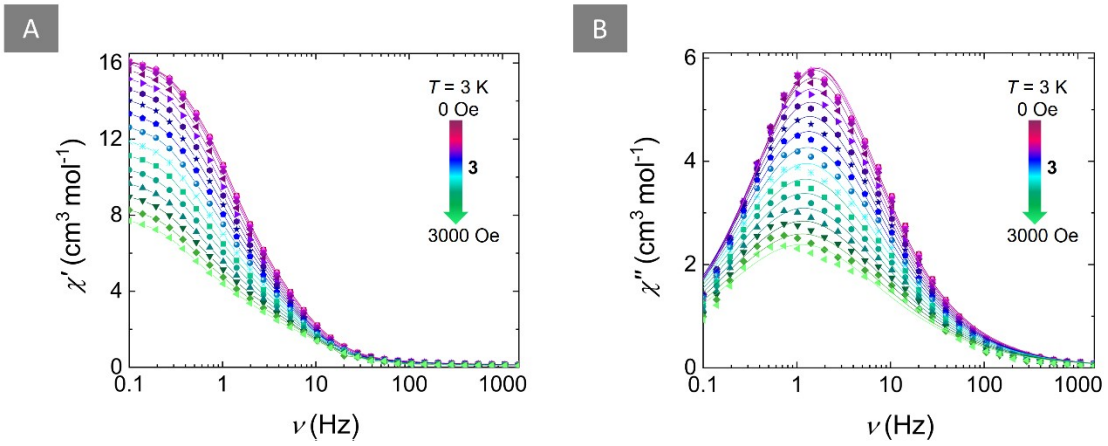

Fig. S17: Field dependence of the in-phase (χ') (A) and out-of-phase (χ'') (B) magnetic susceptibility of **3** at 3 K in the field range of 0 to 3000 Oe. For the χ' the solid lines serve as a guide to the eye, while for the χ'' the solid lines represent the best fit to the generalized Debye model.

Table S7. Best-fit parameters to the generalized Debye model for the frequency dependence of the out-of-phase-magnetic susceptibility (χ'') as a function of field for **3** collected at T = 3 K (Figure S17).

H (Oe)	τ (s)	α	χ_s (cm^3 mol^{-1})	χ_t (cm^3 mol^{-1})
0	9.63 x 10^{-2}	0.24	6.27 x 10^{-2}	17.1
100	9.65 x 10^{-2}	0.24	6.45 x 10^{-2}	17.1
200	9.76 x 10^{-2}	0.24	6.27 x 10^{-2}	17.1
300	9.95 x 10^{-2}	0.23	6.04 x 10^{-2}	17.0
400	1.01 x 10^{-1}	0.23	5.60 x 10^{-2}	17.0
600	1.06 x 10^{-1}	0.24	4.33 x 10^{-2}	16.6
800	1.09 x 10^{-1}	0.25	2.54 x 10^{-2}	16.2
1000	1.12 x 10^{-1}	0.26	1.26 x 10^{-2}	15.7
1200	1.16 x 10^{-1}	0.27	6.46 x 10^{-3}	15.2
1400	1.18 x 10^{-1}	0.28	5.64 x 10^{-3}	14.5
1600	1.22 x 10^{-1}	0.29	6.32 x 10^{-3}	13.8
1800	1.25 x 10^{-1}	0.31	1.37 x 10^{-3}	13.1
2000	1.29 x 10^{-1}	0.32	1.51 x 10^{-3}	12.3
2200	1.32 x 10^{-1}	0.33	1.02 x 10^{-4}	11.6
2400	1.34 x 10^{-1}	0.34	5.72 x 10^{-3}	10.8
2600	1.37 x 10^{-1}	0.35	7.02 x 10^{-3}	10.1
2800	1.39 x 10^{-1}	0.36	7.05 x 10^{-3}	9.38
3000	1.41 x 10^{-1}	0.37	4.92 x 10^{-3}	8.78

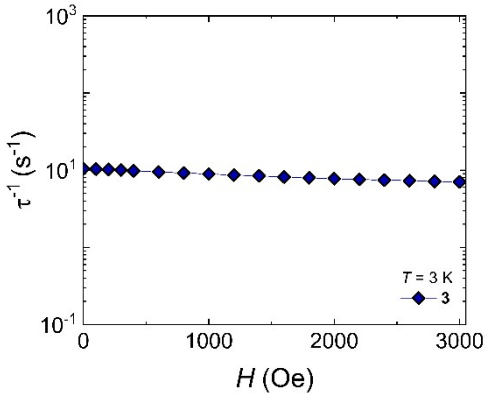

Fig. S18: Field-dependence of the relaxation times (τ) for **3** at a fixed temperature of 3 K. The relaxation times were obtained from the generalized Debye model (*see*, Table S7).

Table S8. Best-fit parameters of the relaxation times of the magnetization for **2** and **3** in the absence and presence of a dc field (1400 Oe).

		2		**3**
		H_{dc} = 0 Oe	H_{dc} = 1400 Oe	H_{dc} = 0 Oe
QTM	τ_{QTM} (s)	0.20		
Orbach	τ_0 (s)	2.51 x 10^{-8}	1.26 x 10^{-8}	5.01 x 10^{-7}
	U_{eff} (cm^{-1})	49.3	52.1	25.0

5. Computational details

The geometries used in the calculations were extracted from the crystal structure. The non-coordinated $[BPh_4]^-$ anions were removed from the structure. The positions of the hydrogen atoms were optimized using density functional theory (DFT) while the positions of the heavier atoms were kept frozen to their crystal-structure coordinates. The geometry optimizations were carried out using the *Amsterdam Density Functional* (ADF) code[16] of the *Amsterdam Modeling Suite* (AMS) version 2020.101.[17] The pure GGA exchange-correlation (XC) functional PBE[18] was used along with the empirical DFT-D3 dispersion correction[19] utilizing the Becke–Johnson (BJ) damping function.[20] Scalar relativistic effects were accounted for using the zeroth-order regular approximation (ZORA) as implemented in ADF.[21] A polarized double-ζ quality basis (DZP) specifically designed for ZORA calculations was used for all atoms.[22] In order to avoid convergence issues and to simulate static correlation effects in the density, the unpaired 4*f* electrons were equally distributed over the seven 4*f* orbitals of the two ions resulting into fractional orbital occupation numbers for **2** and **3**. In practice, this means fixing the occupations of the fourteen highest-lying β orbitals as 0.14286 for **2** and 0.28571 for **3**.

Broken-symmetry (BS) DFT calculations[23,24] on **1** were carried out using the *Orca* code version 4.2.1.[25] The range-separated hybrid XC functional CAM-B3LYP[26] was used in the BS-DFT calculations. The scalar relativistic effects were treated with ZORA as implemented in Orca.[21,27] A double-polarized triple-ζ quality SARC-ZORA-TZVPP was used for the Gd ions.[28] For the remaining atoms, ZORA-def2 basis sets were used that are re-contractions of the def2 basis sets for ZORA calculations.[29] Polarized triple-ζ quality basis sets (ZORA-def2-TZVP) were used for C, N and O whereas a polarized double-ζ basis (ZORA-def2-SVP) was used for the H atoms. Nature of the BS states was confirmed by visual examination of the spin densities.

State-averaged complete active space self-consistent field (SA-CASSCF) type multireference calculations[30] were carried out using the *Orca* code version 5.0.1.[25,31] In the multireference calculations, one of the Ln(III) ions was replaced by a diamagnetic Y(III) ion so the calculations could be carried out only on a single interacting Ln(III)–radical pair. The active space consisted of the seven metal 4*f* orbitals and all six ligand π-orbitals. Inclusion of all six ligand orbitals into the active space was necessary to introduce sufficient amount of electron correlation effects into the CASSCF wave function. The

states included in the state-averaged treatment included all states that could be constructed by coupling the two lowest-lying spin-doublet ligand states with the highest-spin multiplicity terms of the free respective free Ln(III) ion. The first excited ligand state lies at about 22,000 cm^{-1} which is lower than the ^6P free-ion term of the Dy(III) ion in **3**. Thus, the excited ligand state needs to be included in the calculations on **3**. For the sake of consistency, it was also included in the calculation on **1** and **2**. Overall the states solved in the SA-CASSCF procedure consisted of the two nonet and two septet states arising from the coupling of the ^8S term to the two radical doublets for **1**, 14 octet and 14 sextet states arising from coupling of the ^7F term to the two radical doublets for **2**, and 42 septet and 42 pentet states arising from coupling of the ^6H, ^6F and ^6P terms to the two radical doublets for **3**. Further electron correlation effects were accounted for using the *N*-electron valence state perturbation theory at second order (NEVPT2) in its strongly correlated formulation.[32] To reduce the computational costs, a single set of orbitals were used for all states in the NEVPT2 procedure. The spin state energetics of **1** were also calculated using the quasi-degenerate (QD) formulation of NEVPT2[33] but the results did not lead to significant improvement over the conventional NEVPT2 (see Table S10).

Scalar relativistic effects were treated in the multireference calculations using the standard second-order Douglas–Kroll–Heß (DKH) transformation.[34] Spin-orbit coupling (SOC) was introduced using the quasi-degenerate perturbation theory (QDPT) approach,[35] where the SOC operator is constructed in a basis of the SA-CASSCF eigenstates and diagonalized to yield the final spin-orbit coupled states and their eigenvalues. The SOC operator was constructed using the spin-orbit mean-field (SOMF) approximation.[36] Polarized quadruple-ζ quality SARC2-DKH-QZVP basis sets[37] were used for the lanthanide ions and DKH-def2-TZVP basis sets[29] were used for the remaining atoms. The auxiliary basis sets used in the integral transformations were generated using the"AutoAux" feature in *Orca*.[38]

The matrix representations of the Hamiltonian and components of the magnetic moment operators were extracted from the *Orca* calculation using the file produces as a part of the *SINGLE_ANISO* interface of *Orca*. Further extraction of the parameters and calculation of the magnetic susceptibility was carried out using our own code. The magnetic susceptibility χ_{M} was calculated as a linear susceptibility from the powder magnetization M as $\chi_M = M/B$, where B is the magnetic field strength taken as 0.1 T. The powder magnetization was integrated over a Lebedev–Laikov grid[39] using 86 grid points. The **g** tensors of the low-lying Kramers' doublets (KDs) were calculated following the well-established methodology.[40] The magnetic properties of **2** and **3** were calculated using the approximate Zeeman Hamiltonian:

$$\hat{H}_{\mathrm{Zeeman}} = \mu_{\mathrm{B}}\mathbf{B}\cdot\left(g_J\hat{\mathbf{J}}_{M1} + g_J\hat{\mathbf{J}}_{M2} + g_e\hat{\mathbf{S}}_R\right) \quad (1)$$

Where μ_{B} is the Bohr magneton, g_J and g_e are the Landé and free-electron *g* factors, respectively, $\mathbf{B}$ is the magnetic field, and $\hat{\mathbf{J}}_{M1}$, $\hat{\mathbf{J}}_{M2}$ and $\hat{\mathbf{S}}_R$ are effective spin operators acting on the lanthanide and radical sites. While the Zeeman Hamiltonian was approximate, the matrix elements were taken over the full *ab initio* states.

Extraction of parameters

In the case of **1**, the lack of first-order orbital angular momentum contribution allows the exchange interaction to be described using a Heisenberg–Dirac–van Vleck (HDvV) type Hamiltonian[41]

$$\hat{H}_{\mathrm{HDvV}} = -J_{\mathrm{M-R}}\left(\hat{\mathbf{S}}_{\mathrm{M1}}\cdot\hat{\mathbf{S}}_{\mathrm{R}} + \hat{\mathbf{S}}_{\mathrm{M2}}\cdot\hat{\mathbf{S}}_{\mathrm{R}}\right) - J_{\mathrm{M-M}}\hat{\mathbf{S}}_{\mathrm{M1}}\cdot\hat{\mathbf{S}}_{\mathrm{M2}} \quad (2)$$

where $J_{\mathrm{M-R}}$ and $J_{\mathrm{M-M}}$ are exchange coupling parameters for the metal–radical and metal–metal interactions, respectively, and $\hat{\mathbf{S}}_{\mathrm{M1}}$ is an effective spin operator acting on metal site 1. Due to the inversion symmetry of the complex both metal–radical interactions are identical. The isotropic exchange parameters $J_{\mathrm{M-R}}$ and $J_{\mathrm{M-M}}$ for **1** were calculated using both BS-DFT and multireference calculations. Following the common approach, the BS-DFT states were interpreted as expectation values of an Ising type Hamiltonian[24] of the type

$$\hat{H}_{\mathrm{Ising}} = -J_{\mathrm{M-R}}\left(\hat{S}_{z,\mathrm{M1}}\hat{S}_{z,\mathrm{R}} + \hat{S}_{z,\mathrm{M2}}\hat{S}_{z,\mathrm{R}}\right) - J_{\mathrm{M-M}}\hat{S}_{z,\mathrm{M1}}\hat{S}_{z,\mathrm{M2}} \quad (3)$$

where $\hat{S}_{z,\mathrm{M1}}$ is an effective spin operator acting on the projection of the local spin at metal site 1. In order to extract the parameters, three different spin configurations were considered to produce two unique energy differences. The exchange coupling parameters can be extracted from the energies as

$$J_{\mathrm{M-R}} = \frac{E(\uparrow\uparrow\uparrow) - E(\uparrow\downarrow\uparrow)}{7} \text{ and } J_{\mathrm{M-M}} = \frac{2E(\uparrow\uparrow\downarrow) + E(\uparrow\downarrow\uparrow) - 3E(\uparrow\uparrow\uparrow)}{49} \quad (4)$$

where $E(\uparrow\uparrow\uparrow)$ is an energy of a spin configuration with the spins ordered as metal–radical–metal.

The multireference calculations on **1** were carried out only on a single metal–ligand pair. The exchange parameter was extracted directly from the energy difference between the lowest nonet and lowest septet states using the well-established formula:

$$J_{\mathrm{M-M}} = \frac{E(\uparrow\downarrow) - E(\uparrow\uparrow)}{4} \quad (5)$$

In case of **2** and **3** the strong magnetic anisotropy arising from first-order orbital contributions to the magnetic moment, requires a much more complicated form of the exchange coupling Hamiltonian. The metal–radical exchange interaction can be described using a pseudospin operator constructed from equivalent operators in the form[42]

$$\tilde{H} = \sum_{kq} \sum_{k'q'} \mathcal{J}_{kqk'q'} \hat{O}_{kq}(\tilde{\mathbf{J}}) \hat{O}_{k'q'}(\tilde{\mathbf{S}}) \quad (6)$$

where $\mathcal{J}_{kqk'q'}$ is a generalized exchange parameter and $\hat{O}_{kq}(\tilde{\mathbf{J}})$ is an equivalent operator of rank k and component q constructed from a pseudospin operator $\tilde{\mathbf{J}}$ acting on the lanthanide. The pseudospin operator has the same dimension as the ground multiplet of the free lanthanide ion. The equivalent operator $\hat{O}_{k'q'}(\tilde{\mathbf{S}})$ acts on the radical site. The summation over the ranks is carried out so that $k \leq 2\tilde{J}$ and $k'q \leq 2\tilde{S}$. We use equivalent operators as defined by Iwahara and Chibotaru.[42,43] Note that we have included the denominator used by Iwahara and Chibotaru into the definition of the operator; thus, the notation of Iwahara and Chibotaru simplifies as $\hat{O}_{kq}(\tilde{\mathbf{J}})/O_{kq}(\tilde{J}) \rightarrow \hat{O}_{kq}(\tilde{\mathbf{J}})$.

The exchange parameters $\mathcal{J}_{kqk'q'}$ can be extracted using the orthogonality of the equivalent operators:[42]

$$\mathcal{J}_{kqk'q'} = (-1)^{q+q'} \frac{(2k+1)(2k'+1)}{(2\tilde{J}+1)(2\tilde{S}+1)} \left(C^{\tilde{J}\tilde{J}}_{\tilde{J}\tilde{J},k0} C^{\tilde{S}\tilde{S}}_{\tilde{S}\tilde{S},k'0} \right)^2 \mathrm{Tr}\left[\hat{O}_{k-q}(\tilde{\mathbf{J}}) \hat{O}_{k'-q'}(\tilde{\mathbf{S}}) \bar{H} \right] \quad (7)$$

where $C^{\tilde{J}\tilde{J}}_{\tilde{J}\tilde{J},k0}$ and $C^{\tilde{S}\tilde{S}}_{\tilde{S}\tilde{S},k'0}$ are Clebsch–Gordan coefficients within the Condon–Shortley phase convention[44] and $\bar{H}$ is a matrix representation of the electronic Hamiltonian downfolded onto a basis of pseudospin states $|\tilde{J}M_J\rangle \otimes |\tilde{S}M_S\rangle$. The trace is taken over the pseudospin basis. The matrix can be obtained from a matrix representation of the *ab initio* electronic Hamiltonian once the *ab initio* eigenstates have been mapped to the pseudospin states $|\tilde{J}M_J\rangle \otimes |\tilde{S}M_S\rangle$. This is a non-trivial task. Following the approximate definition of pseudospin established by Chibotaru[45] and applied by Ungur and Chibotaru in the *ab initio* crystal-field approach,[46] the pseudospin state can be approximately mapped, up to a phase, to the eigenstates of the component of magnetic moment along the quantization axis. The quantization axis is chosen as the principal magnetic axis of the ground Kramers' doublet (KD). This axis can be unambiguously determined.[40,45] The approximation is valid when the higher-rank contributions to the magnetic moment can be neglected. This is true when the pseudospin closely resembles the true angular momentum of the system as is the case in a system of a lanthanide ion described by a J multiplet that is reasonably well described within *LS* coupling and an isotropic radical spin. The mapping of individual states can be achieved by comparing the *ab initio* eigenvalue of the magnetic moment operator along the quantization axis with a theoretical value calculated using the usual operator form

$$\hat{\mu}_z = -\mu_{\mathrm{B}} \left(g_J \hat{J}_z + g_e \hat{S}_z \right) \quad (8)$$

where the operators are physical operators not pseudospin operators. In the case of Tb(III) and Dy(III) (but not Gd(III)), there are no accidental degeneracies in the eigenvalues, and the mapping can be carried out unambiguously. The differences between the *ab initio* and theoretical eigenvalues in **2** and **3** are always less than $0.04\mu_{\mathrm{B}}$ whereas the spacing between the eigenvalues is always more than $0.20\mu_{\mathrm{B}}$. Thus, the mapping is unambiguous in practice as well.

The mapping can, however, only be carried out up to a phase that is specific to both the *ab intio* state $|\psi_{M_J M_S}\rangle$ and the pseudospin states $|\tilde{J}M_J\rangle$ and $|\tilde{S}M_S\rangle$. Thus, the total phase problem has the form

$$e^{i\theta_{M_J M_S}}|\tilde{\psi}_{M_J M_S}\rangle = e^{i\phi_{M_J}}|\tilde{J}M_J\rangle \otimes e^{i\phi_{M_S}}|\tilde{S}M_S\rangle \quad (9)$$

which cannot be trivially solved as the *ab initio* eigenstates cannot be trivially decomposed into the components of the direct product. The lack of available phase factors means that the time-reversal operator will have a non-trivial phase factor when applied on the pseudospin operators, and this means that the resulting equivalent operator expansion does not have a trivial behavior under time reversal. In practice this means that both equivalent operators of odd and even ranks enter expansion of both time-even and time-odd operators. This makes the interpretation of the individual exchange parameters rather useless. The approach does, however, allow the construction of matrix representations of pseudospin operators and the resulting eigenvalues are correct. Solving the phase issue will be considered in future work.

Properties that depend on the eigenvalues of the Hamiltonian, such as the magnetic susceptibility, can be constructed using the full pseudospin Hamiltonian including both metal–radical interactions and the parameters extracted from the metal–radical pair calculations:

$$\tilde{H} = \sum_{kq}\sum_{k'q'} \mathcal{J}_{kqk'q'}\left(\hat{O}_{kq}(\tilde{\mathbf{J}}_1)\hat{O}_{k'q'}(\tilde{\mathbf{S}}) + \hat{O}_{kq}(\tilde{\mathbf{J}}_2)\hat{O}_{k'q'}(\tilde{\mathbf{S}})\right) . \quad (10)$$

Inclusion of the metal–metal interaction using a point-dipole approximation was also considered, but the dipolar coupling two to three order of magnitude weaker than the metal–radical exchange interaction, and it can be safely neglected.

Data tables and figures

Table S9. Energies of the broken-symmetry states used in the calculation of the exchange coupling parameters for **1**.

Spin configuration[a]	Energy / Hartree
↑↑↑	–25369.7844046123
↑↓↑	–25369.7847470053
↑↑↓	–25369.7850735380

[a] Ordered as Gd–radical–Gd.

Table S10. Energies of the multireference spin states used in the calculation of the exchange coupling parameters for **1**.

Method	*E*(↑↑)[a] / Hartree	*E*(↑↓)[a] / Hartree
CASSCF	–16949.9740073782	–16949.9739909339
NEVPT2	–16961.81916070030275	–16961.81938487140360
QD-NEVPT2	–16961.81609961352660	–16961.81633244668410

[a] Ordered as Gd–radical. The other Gd ion is replaced by Y.

Table S11. Energies and properties of the **g** tensors calculated for the four lowest-lying Kramers doublets calculated for **2**.

E / cm^{-1}	g_X	g_Y	g_Z	θ[a]
0	0.000	0.543	33.777	
38	0.000	0.000	3.803	90.5°
42	0.000	0.000	2.213	90.3°
65	0.000	2.862	30.775	2.8°

[a] The angle between the principal magnetic axes of this KD and the ground KD.

Table S12. Energies and properties of the **g** tensors calculated for the four lowest-lying Kramers doublets calculated for **3**.

E / cm^{-1}	g_X	g_Y	g_Z	θ[a]
0	0.000	0.152	37.331	
21	0.000	0.000	1.954	27.9°
21	0.000	0.000	1.970	29.2°
42	0.000	0.043	41.342	0.2°

[a] The angle between the principal magnetic axes of this KD and the ground KD.

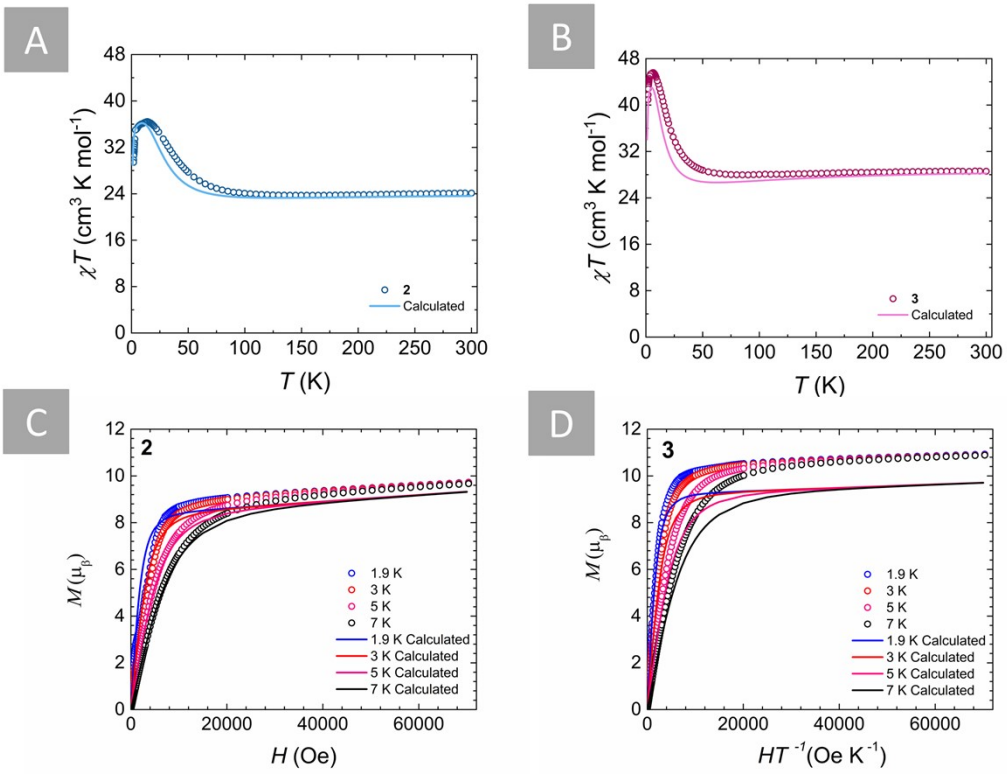

Figure S19. Top: the measured (circles) and calculated (solid lines) magnetic susceptibilities of **2** (A) and **3** (B). Bottom: Measured (circles) and calculated (solid lines) field-dependent low-temperature magnetization of **2** (C) and **3** (D).

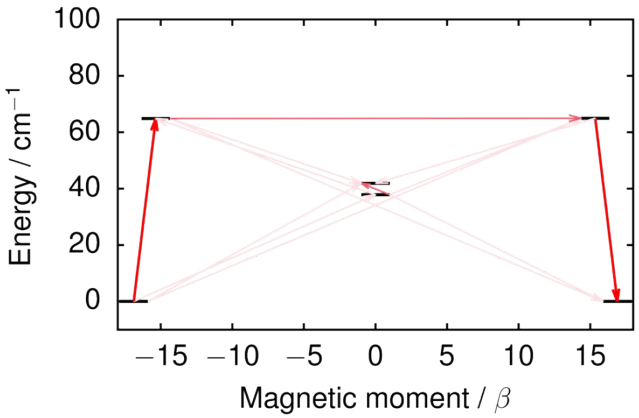

Figure S20. Qualitative barrier for the relaxation of magnetization in **2**. Stronger arrows indicate stronger magnitudes of transition magnetic moment matrix elements between the respective states.

6. References

[1] K. V. Domasevitch, I. A. Gural′skiy, P. V. Solntsev, E. B. Rusanov, H. Krautscheid, J. A. K. Howard and A. N. Chernega, *Dalton Trans.*, **2007**, 3140–3148.

[2] S. Demir, J. M. Zadrozny, M. Nippe and J. R. Long, *J. Am. Chem. Soc.*, **2012**, *134*, 18546–18549.

[3] G. M. Sheldrick, SADABS, *Bruker/Siemens Area Detector Absorption Correction Program V.2.0.3*, Bruker AXS: Madison, WI, **2003**.

[4] G. M. Sheldrick, *Acta Crystallogr. Sect. A: Found. Adv.*, **2015**, *A71*, 3–8.

[5] G. M. Sheldrick, *SHELXL 2018/3: Programme for Crystal structure refinement, Acta Crystallogr. Sect. C.*, **2015**, *C71*, 3–8.

[6] A. L. Spek, *Acta Crystallogr.*, **2015**, *C71*, 9–18.

[7] A. L. Spek, *Acta Crystallogr.*, **1990**, *A46*, C34.

[8] L. J. Farrugia, *J. Appl. Crystallogr.*, **1999**, *32*, 837–838.

[9] K. Brandenburg, *DIAMOND: Program for Crystal and Molecular Structure Visualization*, Crystal Impact GbR, Bonn, Germany, **2014**.

[10] C. F. Macrae, P. R. Edgington, P. McCabe, E. Pidcock, G. P. Shields, R. Taylor, M. Towler and J. van de Streek, *J. Appl. Crystallogr.*, **2006**, *39*, 453–457.

[11] G. R. Desiraju, *J. Chem. Soc. Dalton Trans.*, **2000**, 3745–3751.

[12] J. J. McKinnon, A. S. Mitchell and M. A. Spackman, *Chem. Eur. J.*, **1998**, *4*, 2136–2141.

[13] M. J. Turner, J. J. McKinnon, S. K. Wolff, D. J. Grimwood, P. R. Spackman, D. Jayatilaka and M. A. Spackman, CrystalExplorer17, University of Western Australia, Australia, **2017**.

[14] M. A. Spackman and J. J. McKinnon, *Cryst. Eng. Comm.*, **2002**, *4*, 378–392.

[15] D. Reta and N. F. Chilton, *Phys. Chem. Chem. Phys.*, **2019**, *21*, 23567-23575.

[16] a) ADF 2021.1, SCM, Theoretical Chemistry, Vrije Universiteit, Amsterdam, The Netherlands, http://www.scm.com. E. J. Baerends, T. Ziegler, A. J. Atkins, J. Autschbach, O. Baseggio, D. Bashford, A. Bérces, F. M. Bickelhaupt, C. Bo, P. M. Boerrigter, C. Cappelli, L. Cavallo, C. Daul, D. P. Chong, D. V. Chulhai, L. Deng, R. M. Dickson, J. M. Dieterich, F. Egidi, D. E. Ellis, M. van Faassen, L. Fan, T. H. Fischer, A. Förster, C. Fonseca Guerra, M. Franchini, A. Ghysels, A. Giammona, S. J. A. van Gisbergen, A. Goez, A. W. Götz, J. A. Groeneveld, O. V. Gritsenko, M. Grüning, S. Gusarov, F. E. Harris, P. van den Hoek, Z. Hu, C. R. Jacob, H. Jacobsen, L. Jensen, L. Joubert, J. W. Kaminski, G. van Kessel, C. König, F. Kootstra, A. Kovalenko, M. V. Krykunov, P. Lafiosca, E. van Lenthe, D. A. McCormack, M. Medves, A. Michalak, M. Mitoraj, S. M. Morton, J. Neugebauer, V. P. Nicu, L. Noodleman, V. P. Osinga, S. Patchkovskii, M. Pavanello, C. A. Peeples, P. H. T. Philipsen, D. Post, C. C. Pye, H. Ramanantoanina, P. Ramos, W. Ravenek, M. Reimann, J. I. Rodríguez, P. Ros, R. Rüger, P. R. T. Schipper, D. Schlüns, H. van Schoot, G. Schreckenbach, J. S. Seldenthuis, M. Seth, J.G. Snijders, M. Solà, M. Stener, M. Swart, D. Swerhone, V. Tognetti, G. te Velde, P. Vernooijs, L. Versluis, L. Visscher, O. Visser, F. Wang, T. A. Wesolowski, E. M. van Wezenbeek, G. Wiesenekker, S. K. Wolff, T. K. Woo, A. L. Yakovlev; b) G. te Velde, F. M. Bickelhaupt, E. J. Baerendes, C. Fonseca Guerra, S. J. A. Gisbergen, J. G. Snijders, T. Ziegler, *J. Comp. Chem.*, **2001**, *22*, 931–967; c) C. Fonseca Guerra, J. G. Snijders, G. te Velde, E. J. Baerends, *Theor. Chem. Acc.,* **1998**, *99*, 391–403.

[17] AMS 2021.1, SCM, Theoretical Chemistry, Vrije Universiteit, Amsterdam, The Netherlands, http://www.scm.com. R. Rüger, M. Franchini, T. Trnka, A. Yakovlev, E. van Lenthe, P. Philipsen, T. van Vuren, B. Klumpers, T. Soini.

[18] a) J. P. Perdew, K. Burke, M. Ernzerhof, *Phys. Rev. Lett.*, **1996**, *77*, 3865–3868; b) J. P. Perdew, K. Burke, M. Ernzerhof, *Phys. Rev. Lett.*, **1996**, *78*, 1396.

[19] S. Grimme, J. Antony, S. Ehrlich, H. Krieg, *J. Chem. Phys.*, **2010**, *132*, 154104.

[20] S. Grimme, S. Ehrlich, L. Goerigk, *J. Comp. Chem.*, **2011**, *32*, 1456–1465.

[21] ZORA, general

[22] E. van Lenthe, E. J. Baerends, *J. Comp. Chem.*, **2003**, *24*, 1142–1156.

[23] a) L. Noodleman, *J. Chem. Phys.*, **1981**, *74*, 5737–5743; b) G. Jonkers, C. A. Lange, L. Noodleman, E. J. Baerends, *Mol. Phys.*, **1982**, *46*, 609–620; c) L. Noodleman, J. G. Norman Jr., J. H. Osborne, A. Aizman, D. A. Case, *J. Am. Chem. Soc.*, **1985**, *107*, 3418–3426; d) L. Noodleman, E. R. Davidson, *Chem. Phys.*, **1986**, *109*, 131–143.

[24] a) I de P. R. Moreira, F. Illas, *Phys. Chem. Chem. Phys.*, **2006**, *8*, 1645–1659; b) H. Xiang, C. Lee, H.-J. Koo, X. Gong, M.-H. Whangbo, *Dalton Trans.*, **2013**, *42*, 823–853.

[25] a) F. Neese, *WIREs Comput. Mol. Sci.*, **2017**, *8*, e1327; b) F. Neese, F. Wennmohs, U. Becker, C. Riplinger, *J. Chem. Phys.*, **2020**, *152*, 224108.

[26] a) T. Yanai, D. P. Tew, N. C. Handy, *Chem. Phys. Lett.*, **2004**, *393*, 51–57; b) A. D. Becke, *Phys. Rev. A.*, **1988**, *38*, 3098–3100; c) C. Lee, W. Yang, R. G. Parr, *Phys. Rev. B.*, **1988**, *37*, 785–789.

[27] C. van Wüllen, *J. Chem. Phys.*, **1998**, *109*, 392–399.

[28] D. A. Pantazis, F. Neese, *J. Chem. Theory Comput.*, **2009**, *5*, 2229–2238.

[29] a) D. A. Pantazis, X.-Y. Chen, C. R. Landis, F. Neese, *J. Chem. Theory Comput.*, **2008**, *4*, 908–919; b) F. Weigend, R. Ahlrichs, *Phys. Chem. Chem. Phys.*, **2005**, *7*, 3297–3305.

[30] a) B. O. Roos in *Advances in Chemical Physics, Ab Initio Methods in Quantum Chemistry II*, Vol. 69 (Ed.: K. P. Lawley), Wiley, New York, **1987**, pp. 399–455; b) P. Siegbahn, A. Heiberg, B. Roos, B. Levy, *Phys. Scripta*, **1980**, *21*, 323–327; c) B. O. Roos, P. R. Taylor, P. E. M. Siegbahn, *Chem. Phys.*, **1980**, *48*, 157–173; d) P. E. M. Siegbahn, J. Almlöf, A. Heiberg, B. Roos, *J. Chem. Phys.*, **1981**, *74*, 2384–2396; e) B. O. Roos, R. Lindh, P. Å. Malmqvist, V. Veryazov, P.-O. Widmark, *Multiconfigurational Quantum Chemistry*, Wiley, Hoboken, NJ, **2016**.

[31] F. Neese, *J. Comp. Chem.*, **2022**, in press.

[32] a) C. Angeli, R. Cimiraglia, S. Evangelisti, T. Leininger, J.-P. Malrieu, *J. Chem. Phys.*, **2001**, *114*, 10252–10264; b) C. Angeli, R. Cimiraglia, J.-P. Malrieu, *Chem. Phys. Lett.*, **2001**, *350*, 297–305; c) C. Angeli, R. Cimiraglia, J.-P. Malrieu, *J. Chem. Phys.*, **2002**, *117*, 9138–9153.

[33] a) L. Lang, K. Sivalingam, F. Neese, *J. Chem. Phys.*, **2020**, *152*, 014109; b) C. Angeli, S. Borini, M. Cestari, R. Cimiraglia, *J. Chem. Phys.*, **2004**, *121*, 4043–4049; c) H. Nakano, *J. Chem. Phys.*, **1993**, *99*, 7983–7992.

[34] a) M. Douglas, N. M. Kroll, *Ann. Phys.*, **1974**, *82*, 89–155; b) B. A. Heß, *Phys. Rev. A.*, **1986**, *33*, 3742–3748.

[35] a) F. Neese, T. Petrenko, D. Ganyushin, G. Olbrich, *Coord. Chem. Rev.*, **2007**, *251*, 288–327; b) M. Atanasov, D. Aravena, E. Suturina, E. Bill, D. Maganas, F. Neese, *Coord. Chem. Rev.*, **2015**, *289–290*, 177–214.

[36] a) F. Neese, *J. Chem. Phys.*, **2005**, *122*, 034107; b) A. Berning, M. Shcweizer, H.-J. Werne, P. J. Knowles, P. Palmieri, *Mol. Phys.*, **2000**, *98*, 1823–1833; c) B. A. Heß, C. M. Marian, U. W. Wahlgren, O. Gropen, *Chem. Phys. Lett.*, **1996**, *251*, 365–371.

[37] D. Aravena, F. Neese, D. A. Pantasiz, *J. Chem. Theory Comput.*, **2016**, *12*, 1148–1156.

[38] G. L. Stoychev, A. A. Auer, F. Neese, *J. Chem. Theory Comput.*, **2017**, *13,* 554–562.
[39] V. I. Lebedev, D. N. Laikov, *Dokl. Math.*, **1999**, *59*, 477–481.
[40] L. F. Chibotaru, L. Ungur, *J. Chem. Phys.*, **2012**, *137*, 064112.
[41] O. Kahn, *Molecular Magnetism*, VHC, **1993**.
[42] N. Iwahara, L. F. Chibotaru, *Phys. Rev. B.*, **2015**, *91*, 174438.
[43] N. Iwahara, L. Ungur, L. F. Chibotaru, Phys. Rev. B., **2018**, *98*, 054436.
[44] D. A. Varshalovich, A. N. Moskalev, V. K. Khersonskii, *Quantum Theory of Angular Momentum*, World Scientific Publishing, **1988**.
[45] L. F. Chibotaru in S. A. Rice, A. R. Dinner (Eds.) *Advances in Chemical Physics*, Volume 153, Wiley, **2013**, pp. 397–519.
[46] L. Ungur, L. F. Chibotaru, *Chem. Eur. J.*, **2017**, *23*, 3708–3718.